POLITECNICO DI TORINO
Repository ISTITUZIONALE

Assessment of permeability and microstructural parameters via fractal modelling in bioactive glass-derived scaffolds produced by vat photopolymerization

(Article begins on next page)

04 May 2024

Assessment of permeability and microstructural parameters via fractal modelling in bioactive glass-derived scaffolds produced by vat photopolymerization

Alessandro Schiavi [a], Roberta Gabrieli [b], Gissur Orlygsson [c], Martin Schwentenwein [d], Enrica Verné [b], Francesco Baino [b,*]

[a] *National Institute of Metrological Research (INRiM), Applied Metrology and Engineering Division, 10135 Turin, Italy*
[b] *Institute of Materials Physics and Engineering, Department of Applied Science and Technology (DISAT), Politecnico di Torino, 10129 Turin, Italy*
[c] *Ice Tec, 112 Reykjavik, Iceland*
[d] *Lithoz GmbH, Vienna, Austria*

A B S T R A C T

Porosity-related characteristics of biomedical three-dimensional (3D) scaffolds govern mass transport properties which, in turn, dictate the success of implants in vivo. The accurate determination of permeability and microstructural properties in highly-porous materials – like implantable bone scaffolds – still represents a challenge due to the complex architecture of struts and voids in 3D. In the present study, the complete set of mass transport properties of bioactive glass scaffolds produced by vat photopolymerization was reliably determined by combining experimental assessment, advanced imaging and mathematical modelling based on the Ergun-Wu approach. Specifically, the intrinsic permeability of the scaffolds was experimentally estimated by acoustic measurements, and the pore diameter was calculated through implementing an innovative fractal model. An accurate statistical analysis of the results provided evidence of the robustness of the overall strategy, which can be potentially extended and adapted to the analysis of other types of sintered porous (bio)materials.

1. Introduction

Implantable biomaterials are often designed as three-dimensional (3D) porous templates in order to support living tissue growth and regeneration [1]. This is the typical case of bone tissue engineering, where newly-formed bone can grow inside the pores of biocompatible scaffolds either passively, if almost-inert polymers or metals are used, or even actively by using bioactive glasses or ceramics that exert an osteoinductive action via the release of appropriate ionic species, thus stimulating bone cells towards a path of regeneration and self-repair [2, 3].

In general, it is vital to fully quantify the 3D pore network of scaffolds. The most common parameter that is used to describe the pore network of scaffolds is the total porosity, corresponding to the fraction of empty space (voids) within the material. Total porosity is relatively easy to estimate (for example, by measuring sample mass and geometry) but often provides incomplete information, since it encompasses closed/isolated pores that do not allow fluid to flow or living cells to colonize

the implant [4].

In order to overcome this limitation, a more important parameter was suggested to be the diameter of the interconnects (or windows) between adjacent pores, which are in turn related to scaffold permeability [5]. On the other hand, permeability of bioceramic scaffolds can be directly assessed by either experimental measurements (e.g. by using distilled water [6] or air [7] as working fluids and implementing the Darcy's equation) or numerical calculations (resolution of Stokes equations relevant to the system geometry) [8].

In porous media, permeability quantifies the ability to conduct fluid flow and is affected by a combination of multiple parameters including porosity, pore size (referred to the effective porosity available for fluid flow), pore orientation, tortuosity and interconnectivity. Therefore, permeability is a key parameter in scaffolds for bone tissue engineering as it is related to mass transport properties that can dictate how body fluids penetrate the scaffold as well as the rate of cell migration and vascularization, ultimately affecting bone growth and regeneration. From a general viewpoint, permeability is indeed a function of the

---

* Corresponding author.
  E-mail address: francesco.baino@polito.it (F. Baino).

porosity of a medium but the specific relationship may vary on a case by case base depending on the geometry and characteristics of the pore network [9].

In a couple of previous works, we determined the intrinsic permeability of bioactive glass or hydroxyapatite scaffolds by making use of an acoustic measurement system and used the so-obtained values to estimate the major microstructural parameters of the porous materials after proper modelling the pore configuration in the two systems. In the case of glass scaffolds produced by sacrificial sponge replication [10], a "conventional" foam-like 3D architecture was assumed, and the average diameter of the pore cross-sectional area was directly determined by micro-computed tomography (micro-CT) of the materials. On the contrary, the pore diameter was calculated as a function of the mean trabecular diameter in hydroxyapatite scaffolds produced by vat photopolymerization (VPP), in which the delicate solid skeleton could be described by a fibrous-like structure of sintered struts [11].

The present study deals with the advanced characterization of bioactive glass-derived scaffolds produced by VPP; early morphological analysis by scanning electron microscopy [12] revealed that the pore/thick-strut architecture of such scaffolds cannot be properly described by making use of either the "standard" foam-like or fibrous-like models, but an average diameter of the pore cross-sectional area is estimated through an innovative fractal approach, which is applied here for the first time to a porous biomaterial. This pore diameter value and the intrinsic permeability determined by acoustic method were used as input data to the Ergun-Wu resistance model in order to calculate the complete set of microstructural properties of the scaffolds.

2. Materials and methods

2.1. Theoretical background

The accurate assessment of scaffold microstructural parameters, such as effective porosity, pore tortuosity, pore narrowing ratio, and friction factor, relies on the exploitation of highly reliable experimental data in the Ergun-Wu resistance model [13], as follows (Eq. 1):

$$k_D = \frac{\varphi^2 D_{av}^2 \varepsilon^3}{72\tau(1-\varepsilon)^2} \tag{1}$$

where k_D is the intrinsic Darcian permeability, φ is the true sphericity index of the pore, D_{av} is the average diameter of the pore cross-sectional area, ε is the effective porosity, τ is the pore tortuosity.

The intrinsic Darcian permeability k_D quantifies the ability of a porous material to transmit a fluid (with known dynamic viscosity) in laminar flow regime and the aptitude to retain it due to intrinsic resistive effects; it is expressed in the following form (Eq. 2):

$$k_D = -\mu U \frac{\partial x}{\partial P} \tag{2}$$

where μ is the dynamic viscosity of the fluid, U is the fluid flow velocity through the porous medium in the x-direction, and ∂P is the pressure drop gradient of the fluid flow (upstream and downstream) across the porous medium. In the current study, the Darcian intrinsic permeability is experimentally determined from the pressure wave drop measured by a calibrated acoustic permeameter [14].

It should be noted that Eq. 1 is valid only for fully laminar flow with negligible inertial losses, namely when the interstitial Reynolds number is close to (or less than) unit ($Re_i \approx 1$). The full derivation of the constitutive Eq. (1), based on Forchheimer equation (including viscous and inertial losses) and combined with intrinsic Darcian permeability Eq. (2), is available in [10].

The true sphericity index of the pore is calculated as the ratio of the nominal surface area of a sphere, having the same volume of the object, to the actual surface area of the object, as defined by Wadell [15]. The true pore sphericity index φ ranges from 1 (perfect sphere) to

0 (elongated shape) [16].

The average pore diameter D_{av} represents the actual pore-capillary diameter of Hagen-Poiseuille law within complex randomly-distributed networks of voids. Both the pore sphericity and the diameter of the pore cross-sectional area are determined from micro-CT measurements and computational image analysis.

The effective porosity ε is the fractional volume of the pores allowing fluid flow within the permeable material, excluding voids of dead-end pores, closed pores, interstices or surface roughness that might cause eddies.

The pore tortuosity τ is the ratio between the linear length L_s of the porous material and the actual length L_p of the tortuous pore, i.e. $\tau = L_p/L_s$. Several empirical models are available to calculate pore tortuosity as a function of effective porosity only. In this work, the following empirical relation [17] is used (Eq. 3):

$$\tau = 1 + 0.4\ln\left(\frac{1}{\varepsilon}\right) \tag{3}$$

Once the experimental quantities of Eq. 1 are determined, within the proper expanded uncertainties, the only unknown parameter is the effective porosity. Thus, the expected value of the effective porosity ε can be calculated from the zero-value(s) of the following function (Eq. 4):

$$\frac{72k_D}{\varphi^2 D_{av}^2} = \frac{\varepsilon^3}{(1-\varepsilon)^2} \bullet \frac{1}{1+0.4\ln\left(\frac{1}{\varepsilon}\right)} \tag{4}$$

Besides the pore tortuosity τ (Eq. 3), other microstructural parameters of porous materials can be estimated from the value of the effective porosity, such as the pore narrowing ratio β, the interstitial Reynolds number Re_i, and the friction factor f_c.

The pore narrowing ratio β is determined according to the geometrical model reported by Wu et al. [13,18] (Eq. 5):

$$\beta = \frac{1}{1-\sqrt{1-\varepsilon}} \tag{5}$$

The pore narrowing ratio is a resistive term, which is correlated to the effects of the contraction and expansion of the pore section and can be expressed as the ratio of D_{av} and D_t, namely $\beta = D_{av}/D_t$, where D_t is assumed to be the average diameter of throats.

The interstitial Reynolds number Re_i is calculated form the following relation (Eq. 6):

$$Re_i = \frac{\rho D_{av} U \varphi_p}{\mu(1-\varepsilon)} \tag{6}$$

The interstitial Reynolds number allows quantifying the error, in the Darcy's approach (Eq. 2), due to the nonlinear effects induced by the inertial losses. In particular, if $Re_i \approx 1$, the error in permeability determination (within the linear Darcy's region) is negligible (below 1%); in general, when $Re_i < 10$, the error is below 10% [19,20].

The friction factor f_r provides information about possible incoming turbulent fluid flow induced by the pore surface roughness and pore tortuosity [10]. According to the Ergun-Wu resistance model (Eq. 1), the friction factor is determined from the following relation (Eq. 7):

$$f_c = \frac{72\tau}{Re_i} + 0.75\tau \tag{7}$$

Properly, if the fluid flow is laminar (at very low Reynolds number), the friction factor is independent of the roughness of the pore inner surface. This implies that small irregularities of the surface do not affect the flow through the porous material, e.g. with losses due to the fluid constrained in eddies within the pores, thereby assuring that the intrinsic permeability only depends on the solid phase of the porous material.

2.2. Fabrication of bioactive glass scaffolds

The process followed for scaffold fabrication was comprehensively described in a previous work published by the authors' group [12]. The silicate glass selected for scaffold manufacturing (47.5B glass; composition: 47.5SiO$_2$–10Na$_2$O–10 K$_2$O–10MgO–20CaO-2.5 P$_2$O$_5$ mol.%) [21] was synthesized by a conventional melt-quenching method at 1500 °C starting from a mixture of high-purity oxides and carbonates.

47.5B glass powder was sieved and the particle size fraction below 32 μm was used to prepare the photocurable slurry, which was used as feedstock for the scaffold printing process that was carried out using the CeraFab L30 3D printer (Lithoz GmbH, Vienna, Austria). The used VPP process relies on the selective light exposure of the photocurable glass slurry through a digital mask using the digital light processing (DLP) concept. The printed component geometries were based on a computer-aided design (CAD) virtual model of a 45-ppi commercial polyurethane foam obtained by micro-tomographic imaging, which was used in the format of a stl file as input to the 3D printer. After printing, a multistep thermal treatment was applied to remove the binder (debinding stage at 430 °C for 6 h) and sinter the 47.5B glass particles (650 °C for 1 h) in order to finally obtain foam-like scaffolds.

2.3. Assessment of scaffold permeability

The intrinsic Darcian permeability k_D was measured by means of a calibrated acoustic permeameter, as described in detail in [14]. The permeameter generates very slow pulsations ($\omega \sim 1$ rad/s) of a known air volume V_0 through the porous medium, in order to keep the interstitial Reynolds number low enough to avoid turbulent airflow within the randomly-distributed network of voids. The dynamic pressure wave, generated by an oscillating piston in the air volume, was then measured by means of a capacitive low-frequency pressure field microphone (previously calibrated in the same closed air volume). The pressure wave drop was determined from the ratio ζ between the amplitude of the dynamic pressure wave measured in the hermetically closed air volume (i.e., the microphone sensitivity) and the amplitude of the dynamic pressure wave measured in the same volume of air enclosed by the porous medium. Thus, the intrinsic Darcian permeability k_D was experimentally determined on the basis of the ratio between the r.m.s. volumetric airflow rate and the r.m.s. dynamic pressure, according to Darcy's law for oscillating flows, as follows (Eq. 8):

$$k_D = \mu \frac{q_{v,\text{rms}}}{p_{\text{rms}}} \bullet \frac{L_s}{A_s} \bullet \zeta = \mu \frac{\omega \partial V \left(\sqrt{2}\right)^{-1}}{\gamma p_0 \partial V \left(V_0 \sqrt{2}\right)^{-1}} \bullet \frac{L_s}{A_s} \bullet \zeta = \mu \frac{\omega V_0}{\gamma p_0} \bullet \frac{L_s}{A_s} \bullet \zeta \quad (8)$$

where $q_{v,\text{rms}}$ is the alternating r.m.s. volumetric airflow ($q_{v,\text{rms}} = U \bullet A_s$), p_{rms} is the sinusoidal r.m.s. pressure component depending on the atmospheric static pressure p_0 (with heat capacity ratio $\gamma = 1.4$), ∂V is the volume variation induced by the motion of the piston on the volume of air V_0, L_s is the length of the porous medium (along the flow direction), A_s is the cross-sectional area of the porous medium perpendicular to the flow direction, and ζ is the experimental ratio of the dynamic pressure wave amplitudes as assessed from microphone indications. The dynamic viscosity μ of the air, for acoustic applications, is calculated according to Rasmussen model, using the environmental air temperature T_{air}, the atmospheric pressure p_0, and the relative humidity RH during the measurements as input data [22].

The intrinsic Darcian permeability k_D of the bioactive glass scaffolds was determined from 3 repeated measurements on 7 different samples, in order to take into account both measurement repeatability and reproducibility.

2.4. Micro-computed tomography analysis

Sintered bioactive glass scaffolds were analysed by X-ray micro-CT to allow determination of the diameter of the pore cross-sectional area and the pore sphericity.

Micro-CT scanning of the foam-like scaffolds was performed in air by a Phoenix Nanotom S (Waygate Technologies / Baker Hughes Digital Solutions GmbH, Wunstorf, Germany). Projection images were collected using an acceleration voltage of 80 kV and a source current of 120 μA. A 0.1 mm-thick Cu X-ray filter was employed. The instrument set-up used resulted in a 12.5-fold magnification with a voxel size of 4.00 μm. The rotation step size during data collection was 0.25°, exposure time 2.0 s and tube mode 0. This is the so-called power mode of the instrument with maximum target power of 2.7 W. Four images were integrated for each rotation step and one blank image was collected prior to acquisition of these four images. Reconstruction of the data was performed in the datos-x reconstruction software provided by the equipment manufacturer. Prior to the actual reconstruction, a translational motion compensation was performed to adjust potential mismatching between the 0° and the 360° shadow images in case of a slight movement of the sample during the data collection. Virtual volumes were then reconstructed from the projection images using the datos-x software. The software VGStudio Max 3.3 (Volume Graphics, Heidelberg, Germany) was used for further processing of the data. First, the data were filtered with an adaptive Gaussian filter to eliminate noise. A smoothing factor of 0.8 and an edge threshold of 0.1 were used. The structural features of the scaffolds were determined in the software based on the Cauchy-Crofton approach. Apart from the main software module, the add-on modules Coordinate Measurement and Foam/Powder Analysis were employed. A virtual cylinder with radius of 1.5 mm and length of 5.0 mm was fitted into each reconstructed scaffold model to avoid effects of the irregular contours of the scaffold and establish a basis for the calculations. The cylinder was extracted as a separate virtual volume and an isovalue-based surface determination procedure was run. The Foam/Powder Analysis module was used to extract foam structure data employing a merge threshold of 5% and a standard precision procedure. The analysis direction was along the z-axis (cylinder axis). The purpose of the segmentation algorithm was to divide up connected cells in CT data of foams into single, meaningful cells. Unlike a classic porosity/inclusion analysis, where connected pores are always be regarded as one entity, this allows the analysis of connected cells in a meaningful way. A watershed algorithm was used to determine the cells and the watershed is stopped by the determined surface. The merge threshold determines whether cells are fused or regarded as single cells, with larger thresholds leading to more fusion and smaller thresholds leading to sub-segmentation of cells. A threshold of 100% would merge all open cells into one cell. The module thus allowed the segmentation of CT data into separate cells which can be visualized, quantified and statistically analysed. Data on pore diameter and pore sphericity were extracted accordingly.

2.5. Statistical analysis

The detailed uncertainty budget of Eq. 8, due to the contribution of its constituent physical and mechanical quantities (which are independent variables), is provided by applying the general rule of random error propagation according to GUM [23]; thus, the related expanded uncertainty, with a confidence level of 95% (coverage factor 2) of the intrinsic Darcian permeability $U(k_D)$, is calculated as follows (Eq. 9):

$$U(k_D) = 2\sqrt{\sum_{i=1}^{N} \left(\frac{\partial k_D}{\partial x_i}\right)^2 u^2(x_i)} \quad (9)$$

where x_i is the ith independent variable of Eq. 8, and $u^2(x_i)$ is the standard uncertainty associated to the independent variable x_i.

In Table 1, as an example of calculation (Scaffold #1), each independent variable of Eq. 8 is individually indicated with the related uncertainty $u(x_i)$, the coefficient of sensitivity $\left(\frac{\partial k_D}{\partial x_i}\right)$ and the resulting squared combined uncertainty $u_c^2(y) = \left(\frac{\partial k_D}{\partial x_i}\right)^2 u^2(x_i)$. It should be noted

Table 1
Uncertainty analysis, according to GUM rules (Eq. 9), for a single measurement of intrinsic Darcian permeability related to Sample #1.

Variable x_j	Value	Note	Type of uncertainty	$u(x_i)$	$\frac{\partial k_D}{\partial x_i}$	$u_c^2(y)$
μ /Pa·s	$1.827 \cdot 10^{-5}$	accuracy	B	$1.0 \cdot 10^{-8}$	$1.6 \cdot 10^{-6}$	$8.8 \cdot 10^{-29}$
ω /rad·s^{-1}	0.926	resolution	B	$6.3 \cdot 10^{-3}$	$3.2 \cdot 10^{-11}$	$1.4 \cdot 10^{-26}$
V_0/m^3	$2.49 \cdot 10^{-4}$	repeatability	A	$9.2 \cdot 10^{-7}$	$1.2 \cdot 10^{-7}$	$3.0 \cdot 10^{-27}$
p_0 /Pa	98650	resolution	B	10	$-3.0 \cdot 10^{-16}$	$3.0 \cdot 10^{-30}$
L_s/m	$7.28 \cdot 10^{-3}$	repeatability	A	$2.5 \cdot 10^{-5}$	$4.1 \cdot 10^{-9}$	$2.7 \cdot 10^{-27}$
A_s/m^2	$1.23 \cdot 10^{-5}$	repeatability	A	$1.2 \cdot 10^{-6}$	$-2.4 \cdot 10^{-6}$	$2.1 \cdot 10^{-24}$
$Volt_{cal}$	1.43	repeatability	A	$5.7 \cdot 10^{-4}$	$2.1 \cdot 10^{-11}$	$4.7 \cdot 10^{-29}$
$Volt_{cal}$		resolution	B	$1.0 \cdot 10^{-5}$	$2.1 \cdot 10^{-11}$	$1.4 \cdot 10^{-32}$
$Volt_{test}$	0.87	repeatability	A	$5.1 \cdot 10^{-3}$	$-3.4 \cdot 10^{-11}$	$7.5 \cdot 10^{-27}$
$Volt_{test}$		resolution	B	$1.0 \cdot 10^{-5}$	$-3.4 \cdot 10^{-11}$	$3.9 \cdot 10^{-32}$
k_D /m^2	$2.96 \cdot 10^{-11}$	Variance, u^2				$2.1 \cdot 10^{-24}$
		Standard uncertainty, u				$1.4 \cdot 10^{-12}$
		Degrees of Freedom				102
		Confidence level				95%
		Expanded uncertainty, U_{sample}				$0.29 \cdot 10^{-11}$
		Relative expanded uncertainty				9.7%

that the values of standard uncertainties, $u^2(x_i)$, are calculated either as the square of the experimental standard deviation if the quantity randomly varies (type A uncertainty), or as as the square of half-width of the interval of variability (divided by 3, considering a rectangular distribution) if the quantity is obtained from the manufacturer's specifications and calibration certificates (type B uncertainty).

In detail, the dynamic viscosity of the air μ was determined on the basis of Rasmussen model [22] using as input data the air temperature (23.3 ± 0.1 °C), the relative humidity (57.3 ± 0.1%) and the static atmospheric pressure (98,650 ± 10 Pa) during the measurement. The pulsation ω was measured with a spectrum analyser resolution of 3 mHz; the geometrical dimension of the components of the cavity (of volume V_0), fabricated by means of computerized numerical control machine (CNC) with 1 μm of precision, were determined from a large set of repeated measurements by using a digital calliper (resolution 0.1 μm). Sample height L_s and cross-sectional base area A_s were determined from 3 repeated measurements by using a calibrated digital calliper (resolution 0.1 μm). The output voltage from the microphone (both in calibration and in testing) was determined by taking into account the accuracy from 3 measurement repetitions (i.e., repeatability) and the resolution (10 μV). Finally, the coverage factor ($k = 2$) was attributed on the basis of the effective degrees of freedom ν_{eff} calculated from the Welch-Satterthwaite formula [23–25] and relevant limitations [26] for a confidence level of 95%. According to this approach, the resulting effective degrees of freedom were $\nu_{eff}= 102$.

This statistical analysis was applied to each single bioactive glass scaffold analyzed in this work. Individual experimental values and related uncertainties are reported in detail in Table 2 and Table 3 in the

following Section 3.

3. Results and discussion

3.1. Bioactive glass scaffold geometry

The gross morphology, mechanical properties and in vitro apatite-forming ability of the bioactive glass-derived scaffolds investigated in this work were reported elsewhere; minimal crystallization with almost negligible formation of Ca_2SiO_4 during sintering was also detected [12].

Table 2 collects the physical characteristics of the bioactive glass scaffolds, including the geometrical dimensions in terms of sample height L_s and cross-sectional area A_s, the weight of the solid phase m, the bulk density ρ_{bulk} and the total porosity ε_0, along with the related standard uncertainties. The total porosity ε_0 was determined by gravimetric method according to Eq. 10, as follows:

$$\varepsilon_0 = 1 - \frac{\rho_{bulk}}{\rho_{glass}} \tag{10}$$

where the nominal density of the glass is $\rho_{glass} = 2.64$ g/cm^3 [27].

3.2. Experimental determination of Darcian intrinsic permeability

Table 3 shows the independent variables of Eq. 8 (except for those reported in Table 2) and the corresponding permeability values, along with the related expanded uncertainty, calculated according to Eq. 9. The measurements were carried out in a laboratory with controlled environment temperature, $T_{air}= 23.0 ± 0.5$ °C, at a constant experimental airflow pulsation $\omega = (0.926 \pm 0.003)$ rad/s. The volume of air was $V_0 = (2.498 \pm 0.005) \bullet 10^{-4}$ m^3 and the volumetric airflow was $q_{v,rms} = 1.07 \bullet 10^{-6}$ m^3/s.

From the experimental data shown in Table 3, the overall average intrinsic Darcian permeability was calculated as $\overline{k}_D = 2.70 \bullet 10^{-11}$ with a standard deviation $\sigma = 0.68 \bullet 10^{-11}$ m^2. The overall uncertainty $U(\overline{k}_D)_{overall}$ was determined by taking into account both the standard deviation σ among the experimental results and the individual expanded uncertainty $U(k_D)$, calculated from Eq. 9. Namely, the overall expanded uncertainty was calculated as (Eq. 11):

$$U(\overline{k}_D)_{overall} = 2.48 \sqrt{\left(\frac{U(k_D)_{MAX}}{2}\right)^2 + \sigma^2} \tag{11}$$

where $U(k_D)_{MAX}$ is the maximum values of the expanded uncertainty among the 7 tested bioactive glass scaffolds, namely $U(k_D)_{MAX} = 0.351 \bullet 10^{-11}$ m^2 (Scaffold #4), and σ is the standard deviation. The maximum

Table 2
Bulk and geometrical characteristics of the bioactive glass scaffolds.

Sample #	Height L_s (mm)	Cross-sectional area A_s (mm^2)	Mass m (g)	Bulk density ρ_{bulk} (g/cm^3)	Total porosity ε_0
1	7.277 ± 0.025	12.25 ± 1.52	0.143 ± 0.011	1.600 ± 0.012	0.394 ± 0.028
2	7.077 ± 0.021	12.11 ± 1.40	0.134 ± 0.010	1.567 ± 0.012	0.407 ± 0.029
3	7.737 ± 0.021	11.38 ± 0.44	0.136 ± 0.010	1.540 ± 0.012	0.417 ± 0.030
4	7.785 ± 0.101	11.97 ± 1.48	0.134 ± 0.010	1.436 ± 0.011	0.456 ± 0.032
5	7.635 ± 0.080	11.41 ± 1.10	0.135 ± 0.010	1.551 ± 0.012	0.413 ± 0.029
6	7.400 ± 0.026	12.41 ± 1.04	0.157 ± 0.012	1.705 ± 0.013	0.354 ± 0.025
7	7.297 ± 0.102	12.13 ± 0.45	0.136 ± 0.011	1.541 ± 0.012	0.416 ± 0.030

Table 3
The physical parameter of the Eq. 8 and the related intrinsic Darcian permeability of the 7 bioactive glass scaffolds under investigation.

Sample #	Air viscosity μ (Pa s)	Atmospheric pressure p_0 (Pa)	Sensitivity ratio ζ	Darcian permeability k_D (m^2)	Expanded uncertainty $U(k_D)$ (m^2)
1	$1.827 \cdot 10^{-5}$	98650	1.638	$2.96 \cdot 10^{-11}$	$0.28 \cdot 10^{-11}$
2	$1.829 \cdot 10^{-5}$	98640	1.145	$2.04 \cdot 10^{-11}$	$0.18 \cdot 10^{-11}$
3	$1.829 \cdot 10^{-5}$	98630	1.157	$2.39 \cdot 10^{-11}$	$0.07 \cdot 10^{-11}$
4	$1.829 \cdot 10^{-5}$	98620	1.147	$3.78 \cdot 10^{-11}$	$0.35 \cdot 10^{-11}$
5	$1.830 \cdot 10^{-5}$	98610	1.961	$2.34 \cdot 10^{-11}$	$0.17 \cdot 10^{-11}$
6	$1.830 \cdot 10^{-5}$	98610	1.146	$2.04 \cdot 10^{-11}$	$0.11 \cdot 10^{-11}$
7	$1.830 \cdot 10^{-5}$	98610	1.810	$3.34 \cdot 10^{-11}$	$0.28 \cdot 10^{-11}$

value of the expanded uncertainty is divided by the coverage factor, which in this case is equal to 2, obtained from the inverse of the t-Student distribution with a symmetric confidence level of 95%, and the degrees of freedom, calculated according to the Welch-Satterthwaite formula, as described in Section 2.5. The coverage factor, $k = 2.48$, is obtained by calculating the Student t-factor for $n = 7-1 = 6$ (by considering 7 samples) and 95% symmetric confidence level, according to [28,29]. By taking into account these values, the resulting overall expanded uncertainty is $U(\overline{k_D})_{overall} = 1.74 \bullet 10^{-11}$ m^2.

Fig. 1 reports the experimental data distribution of intrinsic Darcian permeability k_D, along with the individual expanded uncertainties (Eq. 9) and within the overall expanded uncertainties, estimated from Eq. 11 (dotted lines). The thick line is the overall average intrinsic Darcian permeability, namely $\overline{k_D} = 2.70 \bullet 10^{-11}$ m^2. Therefore, the experimental intrinsic Darcian permeability of the bioactive glass scaffolds here investigated can be expressed in the range of $0.96 \bullet 10^{-11}$ - $4.44 \bullet 10^{-11}$ m^2, or as $\overline{k_D} = (2.70 \pm 1.74) \bullet 10^{-11}$ m^2, with a confidence level of 95%.

This permeability range can be compared with previous results reported in the literature, although there is a paucity of specific studies on bioactive glass scaffolds. Ochoa et al. [6] experimentally determined the permeability of 45S5 Bioglass®-derived foam-replicated scaffolds ($1.96 \cdot 10^{-9}$ m^2) by using distilled water as working fluid and by then measuring the pressure drop and fluid flow velocity across the sample to apply the Darcy's equation. Jones et al. [8] estimated the permeability of sol-gel glass foams sintered in the range of 600–1000 °C (7.67–$8.87 \cdot 10^{-10}$ m^2) by making use of micro-CT analysis and numerically solving the relevant Stokes equations. The permeability values reported in these previous studies are from one to two orders of magnitude higher than the range assessed for VPP-produced bioactive glass scaffolds analyzed in the current work. This difference can be explained considering that, although the 3D architectures of current, Ochoa's and Jones' scaffolds are similar (i.e., grossly foam-like structure), the total porosities – and, hence, the effective porosities – are significantly different (85–95 vol% in both previous studies). The same considerations are valid comparing the higher permeability of

hydroxyapatite scaffolds ($0.76 \cdot 10^{-9}$–$1.74 \cdot 10^{-9}$ m^2) produced exactly through the same VPP-based approach in one of our previous works [11]. On the other hand, however, it should also be considered that natural bone permeability may vary over a quite broad range even in the same anatomical site: for example, Nauman et al. [30] reported values from 0.01 to $4.7 \cdot 10^{-9}$ m^2 for human proximal femur, which are comparable to those assessed in the present study.

3.3. Analysis of pore diameter and shape distribution

Micro-CT analysis allowed a detailed quantification of pore diameter D as well as pore shape in terms of sphericity φ. The analysis was carried out on 2 separate bioactive glass scaffolds. Fig. 2 shows selected cross-sections of one of the structures and displays the pore segmentation results. The total number of pore diameters analyzed was 1515.

From micro-CT data extraction, the total volume V_p and the surface area S_p of each pore were individually determined. According to Wadell [15], the true sphericity index was calculated as $\varphi = \sqrt[3]{36\pi V_p^2}/S_p$ and the corresponding diameter as $D = 6V_p/S_p\varphi$.

As illustratively shown in Fig. 3, it is possible to observe that, at a first glance, ~100 pore diameters lie within 0.004 to 0.01 mm, ~900 pore diameters lie within 0.01 to 0.1 mm, and ~500 pore diameters lie within 0.1 mm up to 0.6 mm.

Fig. 4 shows the distribution of the full dataset of pore diameters. The histogram was built with 40 classes (i.e., by applying the square root rule, the number of classes is $\sim \sqrt{1515}$ [31]), having 0.0157 mm of class width. In order to evaluate the average pore diameter D_{av} and the associated uncertainty, several advanced statistical approaches can be applied [32–36], e.g. based on a weighted mean, once a well-defined distribution is available. Indeed, as it will be shown in Section 3.5, simple averaging of the pore diameters (e.g. in terms of arithmetic, geometric, harmonic averaging) is not representative of the actual average pore diameter D_{av}, which is suitable to be applied in Ergun-Wu approach, as the pore diameters distribution acts on the mass transport with different extents: even a small number of large-diameter pores greatly reduces the pressure gradient with respect to the flow resistance produced by the small-diameter pores, since $\Delta p \propto D^{-2}$.

The strong asymmetry of the distribution of pore diameters includes a large number of small diameters in the first 4 classes: 870 diameters lie between 0.004 mm (which is the micro-CT resolution) and 0.067 mm, while the remaining 675 diameters are randomly distributed from 0.067 mm up to 0.632 mm, which is the maximum diameter measured in the dataset.

Fig. 5(a) and (b) depict the pore sphericity distribution and the box-plot analysis, respectively. It can be seen that the average pore sphericity φ can be easily determined from classical statistical approaches: namely, according to the Gaussian approach, the overall average was 0.443 with a standard deviation $\sigma = 0.119$. Similar results can be achieved from box-plot analysis: the median value was 0.430, within 0.37 (1st quartile) and 0.50 (3rd quartile); therefore, hereinafter, the pore sphericity was assumed as $\varphi = 0.443 \pm 0.119$.

In order to estimate the average pore diameter D_{av} and the associated uncertainty, we investigated the suitability of a recently developed fractal analytical model (independent of data distribution) that is only
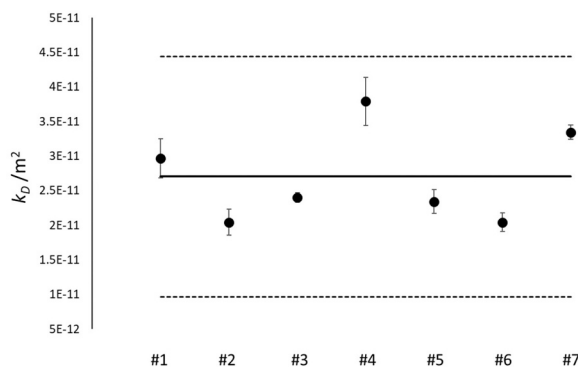

Fig. 1. Experimental data distribution of intrinsic Darcian permeability of scaffolds with the average value (thick line) and overall expanded uncertainty (dotted line).
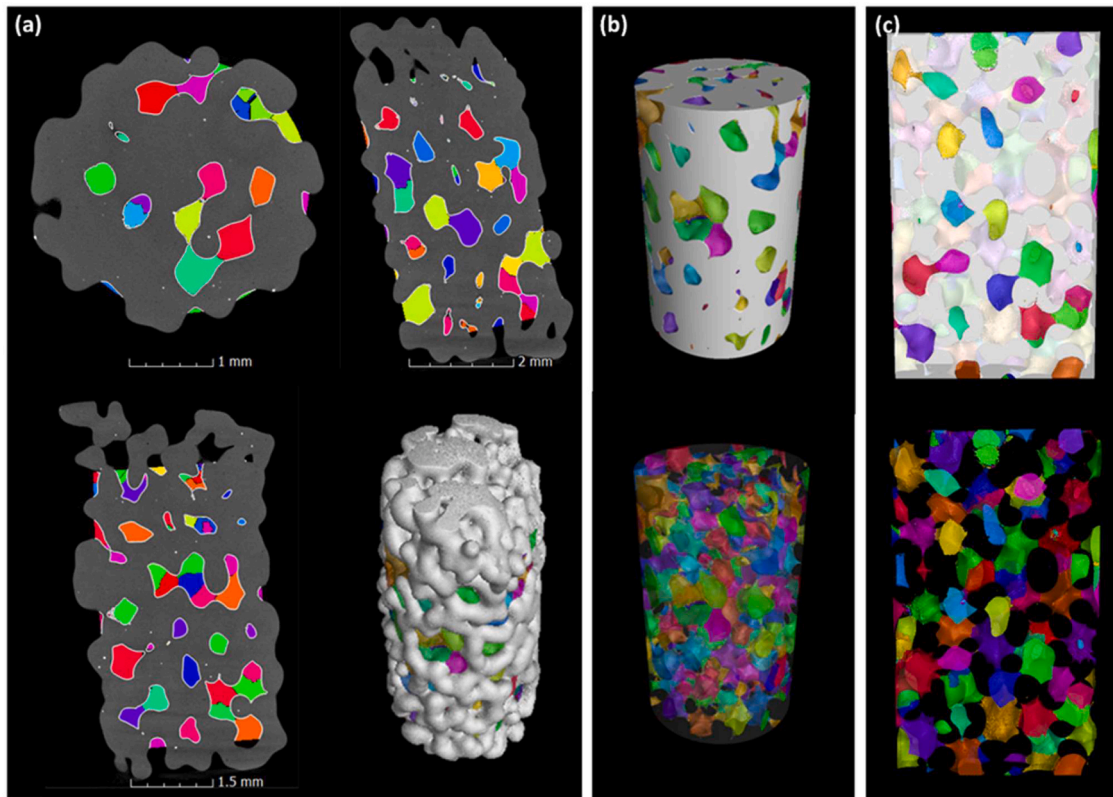
Fig. 2. X-ray micro-CT data extraction. Fig. 2(a) shows three cross-sections through a bioactive glass scaffold (xy, xz and yz planes) and a 3D visualization of the scaffold (bottom right). A virtual cylinder (radius = 1.5 mm, length = 5.0 mm) has been inserted into the structure and a foam structure analysis was performed to extract pore diameter and shape information. Individual pores are shown in discrete colors. Fig. 2(b) shows the virtual cylinder separately with the bioactive glass material displayed as solid (top) or transparent (bottom). Fig. 2(c) shows a view through an approximately 0.75 mm-thick slab from the center of the cylinder and displays further the segmentation of pores in the structure. The glass material is displayed semi-transparent (top) and transparent (bottom). In the top image, openings into the structure appear in saturated colors. In the bottom image the majority of the pores are well separated.
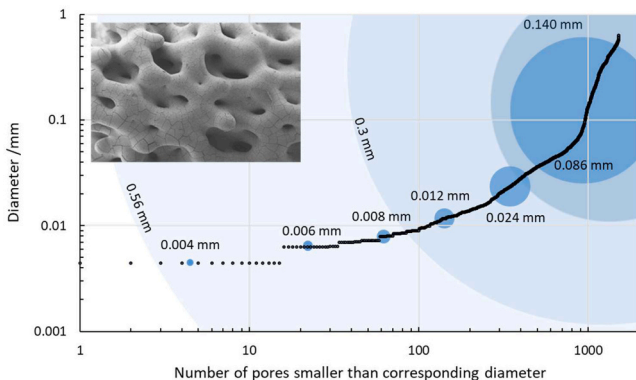

Fig. 3. Diameters of the pore cross-sectional area distribution within the bioactive glass scaffold, with a proportional illustrative comparison of pore cross-sectional area.

based on two experimental input data, i.e. the maximum pore diameter D_{MAX} and the total porosity ε_0. A validation of the model is also proposed in Section 3.5 with respect to traditional statistical approaches.

3.4. Fractal analysis for the determination of average pore diameter

Fractal geometry has been successfully applied both in theoretical and in experimental studies to model peculiar pore diameter distributions for the estimation of the fundamental macroscopic transport properties in porous media [37–41], when modelled on the basis of

Kozeny-Carman relation, and several fractal models were developed accordingly [42–46].

Recently, Xiao *et al.* have derived a novel fractal model for Kozeny-Carman based-approach in converging-diverging capillaries. This model allows providing the average pore diameter also in the case of variable cross-section of pore channel [47]. The fractal model proposed by Xiao *et al.* shows that the average pore diameter D_{av}, where pore diameter is not uniform throughout the porous medium, can be determined from the following relation (after Yun et al. [48]) (Eq. 12):

$$D_{av} = D_{MAX}\left(\frac{d_f}{4 - d_f}\right)^{\frac{1}{4}} \tag{12}$$

where D_{MAX} is the maximum pore diameter and d_f is the pore area fractal dimension with $1 < d_f < 2$; the value of the average pore diameter D_{av} is determined according to a proper fractal scaling law, whose "metric" is defined in the following Eqs. (13) and (14).

According to [45,47], the pore area fractal dimension d_f can be determined from the following analytical formula (Eq. 13):

$$d_f = 2 - \frac{\ln\varepsilon_0}{\ln\alpha} \tag{13}$$

where ε_0 is the total porosity of the bioactive glass scaffold (measured by gravimetric method, as previously described) and α is the structural parameter of the porous medium which can be calculated, according to [38,45,47,49], from (Eq. 14):

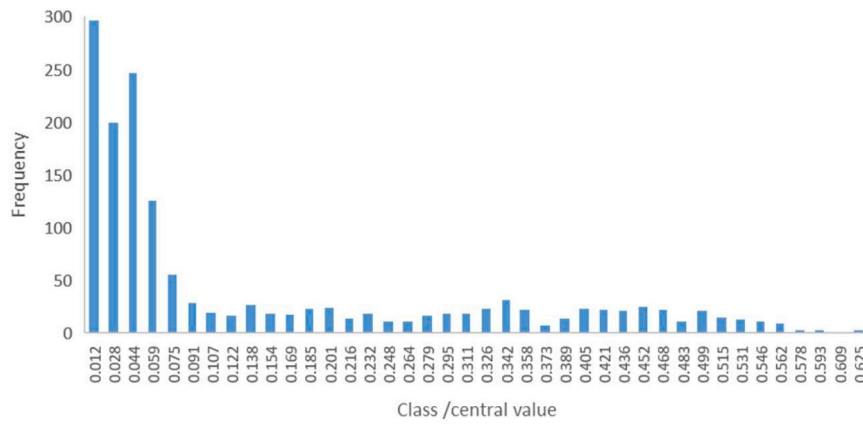$$\alpha = \frac{\sqrt{2(1 - \varepsilon_0)}}{24} \tag{14}$$

Fig. 4. Micro-CT experimental data analysis showing the distribution of pore diameters; each class is indicated with the corresponding central value and the width of each class is 0.0157 mm.
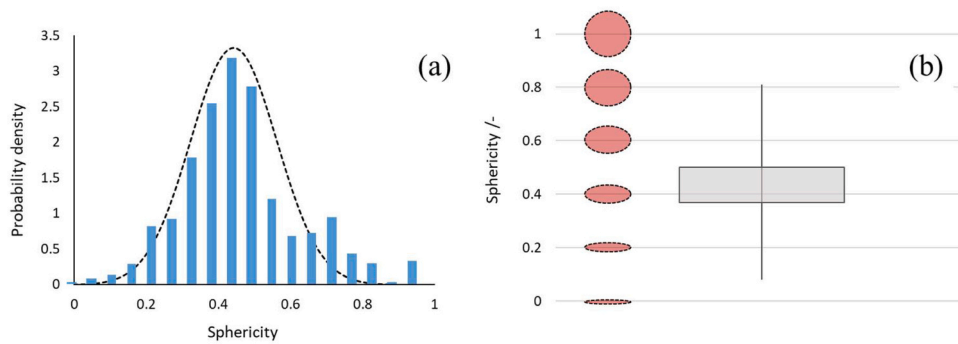

Fig. 5. Micro-CT experimental data analysis: (a) distribution of pore sphericity; (b) box-plot from statistical analysis, with a representation of the corresponding pore sphericity (in red).

If we assume an exact self-similarity of the pores across orders of magnitude in lengths, the structural parameter of the porous medium simply represents the ratio between the maximum and the minimum pore diameter within the porous media (namely, $\alpha = D_{MIN}/D_{MAX}$).

As a matter of fact, however, referring to a statistical self-similarity is preferable for the bioactive glass scaffolds analyzed in the present work since pore diameter and shape can be supposed to exhibit some random/disordered distribution over a certain range of length scales; on the other hand, an exact self-similarity can only be mathematically generated. Nevertheless, according to Xu [50], the fractal scaling law (see Eq. 13 and Eq. 14) can also be applied in porous media showing statistically self-similar characteristics. If so, the fractal scaling law for pore diameter distribution in porous media can be expressed as (Eq. 15):

$$N(D \geq D_{MIN}) = \left(\frac{D_{MAX}}{D_{MIN}}\right)^{d_f} \tag{15}$$

where N represents the number of pores whose diameters are greater than or equal to D_{MIN}, D_{MAX} denotes the maximum pore diameter, and d_f is the fractal dimension for the pore diameter distribution calculated from Eq. 13.

By considering a statistical self-similarity of pores diameter within the analyzed bioactive glass scaffolds, the value of the maximum pore diameter D_{MAX} is defined after an identification of outliers. After being subjected to the Shapiro-Wilk test [51], the experimental data of pore diameter above 0.56 mm were excluded, being considered as outliers (which corresponded to just 13 values, i.e., less than 1% in the overall dataset of 1515 pore diameters analyzed). Thus, hereinafter, the maximum pore diameter of the bioactive glass scaffold was assumed as $D_{MAX} = 0.56 \pm 0.07$ mm. The uncertainty value of 0.07 mm was

attributed in order to take into account the possible variability of the maximum diameter D_{MAX} up to the maximum experimental values actually measured (i.e., 0.632 mm), as shown in Fig. 4.

Once the maximum diameter D_{MAX} has been attributed, the structural parameter of the bioactive glass scaffold α (Eq. 14) and the related pore area fractal dimension d_f (Eq. 13) were calculated accordingly. Finally, the average pore diameter D_{av} (Eq. 12) was derived with its relative expanded uncertainty. These values were separately determined for the 7 bioactive glass scaffolds, as shown in Table 4.

As shown in Table 4, the value of the average pore diameter $D_{av} \cong 0.520$ mm was assumed as the equivalent of pore-capillary diameter in Kozeny-Carman equation, to be exploited in the proposed Ergun-Wu model for the microstructural characterization. The overall expanded uncertainty of the average pore diameter, $U(D_{av})_{overall} = 0.082$ mm, was calculated according to the rule of Eq. 11, where $U(D_{av})_{MAX} = 0.0658$ mm (Scaffold #5), with standard deviation $\sigma = 0.004$mm and coverage factor $k = 2.48$, by considering 7 occurrences, with 95% of symmetric confidence level. The same rule was applied for the calculation of the overall expanded uncertainties of the constituent parameters.

3.5. Validation of the fractal analysis

In order to provide evidence supporting the proposed fractal analysis, two different approaches were investigated. The first is based on the verification of the conditions of statistical self-similarity, the latter relies on a comparison with the weighted mean calculated from the complete dataset of pore diameter distribution.

According to the results shown in Table 4, the minimum pore diameter can be estimated as $D_{MIN} \cong 0.025$ mm (since $\alpha \bullet D_{MAX} = D_{MIN}$), by supposing an exact self-similarity of the pore diameters across

Table 4

Experimental values of the total porosity ε_0, the related porosity-dependent structural parameters, and the average pore diameter D_{av}. Data are expressed with the related expanded uncertainties.

Sample #	Total Porosity ε_0	U (ε_0)	Structural Parameter α	U (α)	Fractal Dimension d_f	U (d_f)	Average Pore Diameter D_{av} (mm)	U (D_{av}) (mm)
1	0.394	0.028	0.0459	0.0011	1.6977	0.0231	0.5190	0.0650
2	0.407	0.029	0.0454	0.0011	1.7089	0.0224	0.5204	0.0652
3	0.417	0.030	0.0450	0.0011	1.7178	0.0217	0.5216	0.0653
4	0.456	0.032	0.0435	0.0011	1.7496	0.0197	0.5211	0.0653
5	0.413	0.029	0.0452	0.0011	1.7142	0.0220	0.5258	0.0658
6	0.354	0.025	0.0474	0.0010	1.6597	0.0260	0.5139	0.0644
7	0.416	0.030	0.0450	0.0011	1.7171	0.0218	0.5215	0.0653
AVERAGE	0.408	0.085	0.045	0.003	1.709	0.074	0.520	0.082

orders of magnitude. On the other hand, by applying Eq. 15 and according to the statistical self-similarity, in order to satisfy the condition $N(D \geq D_{MIN}) = 1515$, with a fractal dimension $d_f \cong 1.709$ and a maximum pore diameter assumed as $D_{MAX} \cong 0.56$ mm, the minimum pore diameter D_{MIN} is ~0.0077 mm. This result, which is close to the minimum pore diameter experimentally measured by the micro-CT (i.e., 0.0044 mm), provides evidence of the suitability of the proposed fractal model to estimate the average pore diameter D_{av}. It means that, at least between $D_{MIN} \cong 0.0077$ mm and $D_{MAX} \cong 0.56$ mm, the pore diameter distribution in the bioactive glass scaffolds follows the proposed fractal scaling law. It should be noted that more than 95% of 1515 measured pore diameters falls within this range.

On the other hand, by exploiting the complete dataset of pore diameter distribution, it is possible to apply several traditional statistical methods to evaluate the average pore diameter D_{av}. Once a well-defined distribution is available, as shown in Section 3.3, a statistical approach, e.g., based on the calculation of the weighted mean, is expected to provide compatible results in compliance with the fractal approach.

The weighted mean was calculated for 3 different distributions, namely the dataset of $N = 1515$ pore diameters was collected in histograms of 40, 20, and 10 classes; the number of classes n was defined according to 3 different rules, i.e. the "square root rule" $n = \sqrt{N}$ [31], the "Scott's rule" $n = 2\sqrt[3]{N}$ [52], and the "Sturges' Rule" $n = 1 + \log_2 N$ [53], respectively.

The weighted mean of pore diameter $\overline{D_n}$ was calculated according to (Eq. 16):

$$\overline{D_n} = \frac{\sum\limits_{i=1}^{n} D_i w_i}{\sum\limits_{i=1}^{n} w_i} \qquad (16)$$

where n is the number of the classes of the considered histogram, D_i is the central value of the pore diameter within the ith class, and the weight w_i was set as the inverse of frequency (i.e., the inverse of the number of occurrences included in the ith class).

The corresponding standard deviations σ_n were calculated as follows (Eq. 17):

$$\sigma_n = \sqrt{\frac{\sum\limits_{i=1}^{n} D_i^2 w_i}{\sum\limits_{i=1}^{n} w_i} - \overline{D_n^2}} \qquad (17)$$

By applying this approach, the following weighted means of the pore diameters (and the related standard deviations) were obtained: $\overline{D_{10}} = 0.465 \pm 0.028$, $\overline{D_{20}} = 0.480 \pm 0.028$, and $\overline{D_{40}} = 0.475 \pm 0.028$. These values are compatible with the average pore diameter calculated from the fractal analysis, namely $D_{av} = 0.520 \pm 0.082$. The compatibility was simply checked from the calculation of the normalized error, as commonly carried out in proficiency tests [54].

As shown in Fig. 6, although the value of the average pore diameter D_{av} calculated by the fractal approach is of about 10% greater than the
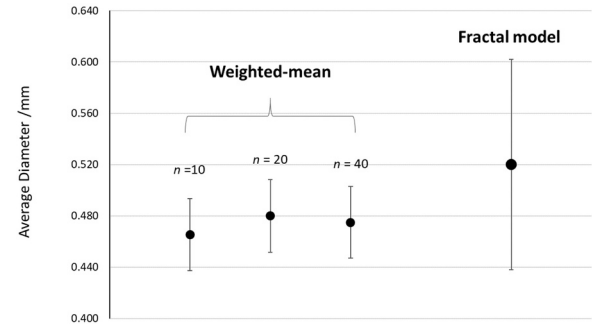

Fig. 6. Comparison among values of pore diameter $\overline{D_n}$ calculated from the weighted mean (for different distributions) and the value of average pore diameter D_{av} calculated by the proposed fractal approach.

values calculated in terms of weighted mean, the range of its expanded uncertainty includes the full variability of $\overline{D_{10}}$, $\overline{D_{20}}$ and $\overline{D_{40}}$. This evidence supports the suitability of result obtained from the fractal analysis.

On the sidelines, as a further checking procedure, it is possible to verify that the thus determined average pore diameter D_{av} is at least greater than a certain threshold value, which can be calculated from the Eq. 4, in order to satisfy the restrictive physical condition $\varepsilon \leq \varepsilon_0$, i.e., the effective porosity ε must always be at lower than the total porosity ε_0. For the bioactive glass scaffolds investigated here, having the Darcian permeability $k_D = 2.70 \bullet 10^{-11}$ m^2, the pore sphericity $\varphi = 0.433$, and the total porosity $\varepsilon_0 = 0.41$, the resulting average pore diameter D_{av} should at least exceed the threshold of 0.263 mm. It should be noted that, in this specific case, simple averaging calculations provide results well below this threshold: for example, the arithmetic mean provides $D_{ar} = 0.144$ mm, the harmonic mean provides $D_{har} = 0.032$ mm and the quadratic mean provides $D_{qu} = 0.002$ mm. Furthermore, the expected values from hypergeometric and binomial distributions show values around the minimum diameter, thus well below the threshold of 0.263 mm. These evidences validate the results previously found with weighted mean and fractal analysis, since both exceed the identified threshold.

3.6. Microstructural and transport properties

The microstructural and transport properties of the bioactive glass scaffolds, as described in Section 2.1, were determined on the basis of the effective porosity value ε; in other words, only the interconnected voids admitting the fluid flow within the solid phase were taken into account. According to the Ergun-Wu relation (Eq. 1), once the experimental quantities (along with their related expanded uncertainties) are known, it is possible to calculate the effective porosity value ε from the zero-value(s) of Eq. 4. The experimental quantities to be introduced in this calculation were the intrinsic Darcian permeability $k_D = (2.70 \pm 1.74) \bullet 10^{-11}$ m^2, the pore sphericity $\varphi = 0.443 \pm 0.119$ and the average

pore diameter $D_{av} \cong 0.520 \pm 0.0658$ mm. By applying the general rule of random error propagation (as shown in Section 2.5), the minimum and the maximum values of the known term of Eq. 4 were calculated with a confidence level of 95%, thus obtaining a Min value of 0.0048 and a Max value of 0.0686. Then the zero-values, corresponding to the minimum and the maximum values of effective porosity of the bioactive glass scaffolds, were determined by graphical solution as shown in Fig. 7.

Once the range of effective porosity has been determined, the microstructural and transport parameters were calculated accordingly, such as pore tortuosity τ (Eq. 3), pore narrowing ratio β (Eq. 5), average diameter of throats D_t, the Reynolds number Re_i (Eq. 6) and the friction factor f_c (Eq. 7). Moreover, the closed porosity ε_c, representing the percentage of pores that do not allow fluid to flow through the scaffold, i.e., $\varepsilon_c = \varepsilon_0 - \varepsilon$, was also calculated.

Table 5 collects the ranges of microstructural and transport properties, calculated from the maximum value ε_{max} and the minimum value ε_{min} of effective porosity.

Among the microstructural parameters mentioned above, tortuosity is known not only to play an obvious role in affecting the fluid flow through the porous network but also to have an impact on the mechanical properties: in this regard, Roque et al. [55] reported that the lower the tortuosity, the higher the strength of human radius cancellous bone. The tortuosity range of VPP-produced glass scaffolds (Table 5) is comparable to the values assessed for ex-vivo samples of distal radius trabecular bone from 15 individuals (1.245–2.154) through applying a geodesic reconstruction algorithm of 3D micro-CT images [56]. On the other hand, hydroxyapatite scaffolds produced by the same virtual template-based additive manufacturing approach exhibit lower tortuosity of pores (1.215–1.239) [11], which may be due to the different sintering/densification behavior resulting in higher (effective) porosity and, as already highlighted, higher permeability.

Furthermore, the evaluation of the pore narrowing ratio is of interest for an adequate understanding of mass transport processes in scaffolds. In fact, in order to optimize some key mechanisms involving implantable scaffolds, e.g. cell seeding and migration, vascularization as well as drug delivery, the knowledge of the (average) narrowings of diameter that may occur in the pores allows avoiding trapping or obstruction phenomena, which would otherwise be underestimated or disregarded if only average pore diameter (within relevant uncertainties) is considered [57–59]. In the bioactive glass scaffolds here investigated, the pore narrowing ratio, calculated according to Eq. 5, ranges between 5.161 and 11.241, which means that, on average, the estimated average pore diameter can have throats that narrow it by 5 up to more than 11 times. Indeed, the average diameter of throats varies between 0.052 and 0.088 mm.

Finally, the interstitial Reynolds number (determined from Eq. 6), ranging between 1.31 and 2.31, indicates that nonlinear effects induced by the inertial losses in permeability measurements are generally below 2% [19,20], thereby guaranteeing the feasibility of the proposed Darcian approach. Moreover, the very high values of friction factor (Eq. 7) show that the flow is fully laminar and free of turbulences [60] within the complex randomly-distributed network of voids of the bioactive glass scaffolds investigated.

4. Conclusions

This work succeeded in achieving two major objectives. The first result is a methodological achievement, i.e., an innovative experimental-theoretical approach was proposed and successfully applied to determine the complete set of mass transport and microstructural properties in 3D porous glass scaffolds. Specifically, it is worth mentioning the good agreement found in terms of pore diameter determined by direct experimental analysis (micro-CT scanning) and fractal modelling. The second achievement concerns the reliable estimation of the microstructural parameters in the case of bioactive glass
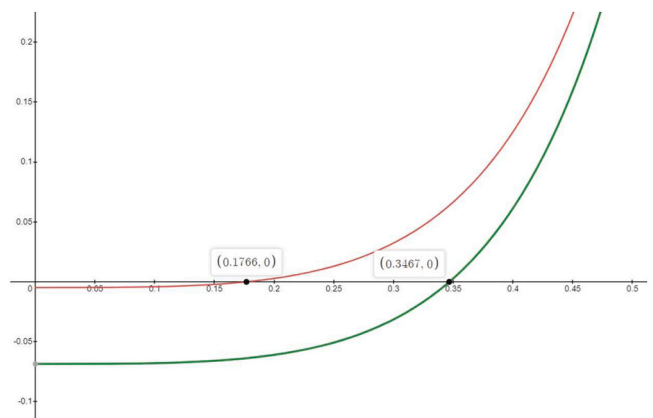

Fig. 7. Graphical solution of Eq. 4, assessed by experimental values of intrinsic Darcian permeability k_D, average pore diameter D_{av} and pore sphericity φ.

Table 5
Summary of microstructural and transport properties ranges.

Microstructural Parameter	Min	Max
Effective porosity ε	0.17	0.35
Closed porosity ε_c	0.06	0.24
Tortuosity	1.420	1.709
Narrowing ratio	5.161	11.241
Throat diameter (mm)	0.052	0.088
Interstitial Reynolds number	1.31	2.31
Friction factor	78.8	54.6

scaffolds produced by VPP. These scaffolds were found to exhibit total porosity of 40.8 ± 3.0 vol% and average pore diameter of 0.520 ± 0.066 mm by applying a fractal model. The Ergun-Wu mathematical approach, supported by micro-CT imaging, was implemented to estimate the effective porosity (17 - 35 vol%), pore tortuosity (1.420 - 1.709) and equivalent throat diameter (0.052–0.088 mm) with a confidence level of 95%. These key microstructural parameters, being comparable to those of human trabecular bone, support the scaffold suitability for bone repair applications.

CRediT authorship contribution statement

Alessandro Schiavi: Conceptualization; Data curation; Formal analysis; Investigation; Methodology; Resources; Supervision; Validation; Writing - original draft; Writing - review & editing. **Roberta Gabrieli:** Investigation; Methodology; Writing - review & editing. **Gissur Orlygsson:** Investigation; Methodology; Writing - review & editing. **Martin Schwentenwein:** Methodology; Resources; Writing - review & editing. **Enrica Verné:** Methodology; Resources; Supervision; Writing - review & editing. **Francesco Baino:** Conceptualization; Investigation; Methodology; Resources; Supervision; Writing - original draft; Writing - review & editing.

Declaration of Competing Interest

The authors declare that they have no known competing financial interests or personal relationships that could have appeared to influence the work reported in this paper.

References

[1] A.A. El-Rashidy, J.A. Roether, L. Harhaus, U. Kneser, A.R. Boccaccini, Regenerating bone with bioactive glass scaffolds: a review of in vivo studies in bone defect models, Acta Biomater. 62 (2017) 1–28.
[2] Viviana Mouriño, Juan Pablo Cattalini, Aldo R. Boccaccini, Metallic ions as therapeutic agents in tissue engineering scaffolds: an overview of their biological

applications and strategies for new developments, J. R. Soc. Interface 9 (2012) 401–419.

[3] U. Pantulap, M. Arango-Ospina, A.R. Boccaccini, Bioactive glasses incorporating less-common ions to improve biological and physical properties, J. Mater. Sci: Mater. Med. 33 (2022) 3.

[4] V. Karageorgiou, D. Kaplan, Porosity of 3D biomaterial scaffolds and osteogenesis, Biomaterials 26 (2005) 5474–5491.

[5] J.R. Jones, R.C. Atwood, G. Poologasundarampillai, S. Yue, P.D. Lee, Quantifying the 3D macrostructure of tissue scaffolds, J. Mater. Sci. Mater. Med 20 (2009) 463–471.

[6] I. Ochoa, J.A. Sanz-herrera, J.M. Garcia-Aznar, M. Doblaré, D.M. Yunos, A. R. Boccaccini, Permeability evaluation of 45S5 bioglass-based scaffolds for bone tissue engineering, J. Biomech. 42 (2009) 257–260.

[7] F. Baino, G. Magnaterra, E. Fiume, A. Schiavi, L.P. Tofan, M. Schwentenwein, E. Verné, Digital light processing stereolithography of hydroxyapatite scaffolds with bone-like architecture, permeability, and mechanical properties, J. Am. Ceram. Soc. 105 (2022) 1648–1657.

[8] J.R. Jones, G. Poologasundarampillai, R.C. Atwood, D. Bernard, P.D. Lee, Non-destructive quantitative 3D analysis for the optimisation of tissue scaffolds, Biomaterials 28 (2007) 1404–1413.

[9] Fabian B. Wadsworth, Jeremie Vasseur, Michael J. Heap, Lucille Carbillet, Donald B. Dingwell, Thierry Reuschlé, Patrick Baud, Universal model for the permeability of sintered materials, Acta Mater. 250 (2023) 118859.

[10] E. Fiume, A. Schiavi, G. Orlygsson, C. Bignardi, E. Verné, F. Baino, Comprehensive assessment of bioactive glass and glass-ceramic scaffold permeability: experimental measurements by pressure wave drop, modelling and computed tomography-based analysis, Acta Biomater. 119 (2021) 405–418.

[11] A. Schiavi, E. Fiume, G. Orlygsson, M. Schwentenwein, E. Verné, F. Baino, High-reliability data processing and calculation of microstructural parameters in hydroxyapatite scaffolds produced by vat photopolymerization, J. Eur. Ceram. Soc. 42 (2022) 6206–6212.

[12] F. Baino, I. Dias, M. Alidoost, M. Schwentenwein, E. Verné, Making foam-like bioactive glass scaffolds by vat photopolymerization, Open Ceram. 15 (2023) 100392.

[13] J. Wu, B. Yu, M. Yun, A resistance model for flow through porous media, Transp. Porous Med. 71 (2008) 331–334.

[14] A. Schiavi, C. Guglielmone, F. Pennella, U. Morbiducci, Acoustic method for permeability measurement of tissue-engineering scaffold, Meas. Sci. Technol. 23 (2012) 105702.

[15] H. Wadell, Volume, shape, and roundness of rock particles, J. Geol. 40 (1932) 443–451.

[16] I. Cruz-Matías, D. Ayala, D. Hiller, et al., Sphericity and roundness computation for particles using the extreme vertices model, J. Comp. Sci. 30 (2019) 28–40.

[17] J. Comiti, M. Renaud, A new model for determining mean structure parameters of fixed beds from pressure drop measurements: application to beds packed with parallelepipedal particles, Chem. Eng. Sci. 44 (1989) 1539–1545.

[18] J. Wu, D. Hu, W. Li, X. Cai, A review on non-Darcy flow—Forchheimer equation, hydraulic radius model, fractal model and experiment, Fractals 24 (02) (2016) 1630001.

[19] M.V. Chor, W. Li, A permeability measurement system for tissue engineering scaffolds, Meas. Sci. Technol. 18 (2007) 208–216.

[20] F. Pennella, G. Cerino, D. Massai, D. Gallo, G. Falvo D'Urso Labate, A. Schiavi, M. A. Deriu, A. Audenino, U. Morbiducci, A survey of methods for the evaluation of tissue engineering scaffold permeability, Ann. Biomed. Eng. 41 (2013) 2027–2041.

[21] E. Verné, O. Bretcanu, C. Balagna, C.L. Bianchi, M. Cannas, S. Gatti, C. Vitale-Brovarone, Early stage reactivity and in vitro behavior of silica-based bioactive glasses and glass-ceramics, J. Mater. Sci. Mater. Med. 20 (2009) 75–87.

[22] K. Rasmussen, Calculation methods for the physical properties of air used in the calibration of microphones, Report No. PL-11b, Technical University of Denmark, Lyngby, Denmark, 1997.

[23] JCGM 100 2008 Evaluation of Measurement Data — Guide to the Expression of Uncertainty in Measurement (GUM), France: Joint Committee for Guides in Metrology, Sèvres).

[24] F.E. Satterthwaite, Synthesis of variance, Psychometrika 6 (5) (1941) 309–316.

[25] F.E. Satterthwaite, An approximate distribution of estimates of variance components, Biom. Bull. 2 (6) (1946) 110–114.

[26] M. Ballico, Limitations of the Welch-Satterthwaite approximation for measurement uncertainty calculations, Metrologia 37 (1) (2000) 61.

[27] E. Fiume, D. Tulyaganov, G. Ubertalli, E. Verné, F. Baino, Dolomite-foamed bioactive silicate scaffolds for bone tissue repair, Materials 13 (2020) 628.

[28] W. Pabst, E. Gregorová, T. Uhlířová, Microstructure characterization via stereological relations—a shortcut for beginners, Mater. Charact. 105 (2015) 1–12.

[29] T. Uhlířová, E. Gregorová, W. Pabst, V. Nečina, Preparation of cellular alumina ceramics via biological foaming with yeast and its microstructural characterization via stereological relations, J. Eur. Ceram. Soc. 35 (1) (2015) 187–196.

[30] E.A. Nauman, K.E. Fong, T.M. Keaveny, Dependence of intertrabecular permeability on flow direction and anatomic site, Ann. Biomed. Eng. 24 (1999) 517–524.

[31] O.L. Davies, P.L. Goldsmith, Statistical Methods in Research and Production, Longman Group Limited, New York, NY, 1980, pp. 166–167.

[32] A.L. Rukhin, Weighted means statistics in interlaboratory studies, Metrologia 46 (3) (2009) 323.

[33] M.G. Cox, C. Eiø, G. Mana, F. Pennecchi, The generalized weighted mean of correlated quantities, Metrologia 43 (4) (2006) S268.

[34] N.F. Zhang, The uncertainty associated with the weighted mean of measurement data, Metrologia 43 (3) (2006) 195.

[35] W. Pabst, S.O. N.A. Hříbalová, Mean values, moments, moment ratios and a generalized mean value theorem for size distributions, Ceram. Silik. 63 (4) (2019) 419–425.

[36] S. Hříbalová, W. Pabst, Transmittance predictions for transparent alumina ceramics based on the complete grain size distribution or a single mean grain size replacing the whole distribution, J. Eur. Ceram. Soc. 42 (12) (2022) 5093–5107.

[37] B. Yu, J. Li, Some fractal characters of porous media, Fractals 9 (03) (2001) 365–372.

[38] B. Yu, Fractal character for tortuous streamtubes in porous media, Chin. Phys. Lett. 22 (1) (2005) 158.

[39] J. Wu, B. Yu, A fractal resistance model for flow through porous media, Int. J. Heat. Mass Transf. 50 (19-20) (2007) 3925–3932.

[40] M. Yun, Seepage characteristics study on power-law fluid in fractal porous media, Math. Probl. Eng. 2014 (2014).

[41] S. Yang, M. Liang, B. Yu, M. Zou, Permeability model for fractal porous media with rough surfaces, Microfluid. Nanofluidics 18 (2015) 1085–1093.

[42] P. Xu, B. Yu, Developing a new form of permeability and Kozeny–Carman constant for homogeneous porous media by means of fractal geometry, Adv. Water Resour. 31 (1) (2008) 74–81.

[43] N. Henderson, J.C. Brêttas, W.F. Sacco, A three-parameter Kozeny–Carman generalized equation for fractal porous media, Chem. Eng. Sci. 65 (15) (2010) 4432–4442.

[44] S. Yang, B. Yu, M. Zou, M. Liang, A fractal analysis of laminar flow resistance in roughened microchannels, Int. J. Heat. Mass Transf. 77 (2014) 208–217.

[45] B. Xiao, W. Wang, X. Zhang, G. Long, J. Fan, H. Chen, L. Deng, A novel fractal solution for permeability and Kozeny-Carman constant of fibrous porous media made up of solid particles and porous fibers, Powder Technol. 349 (2019) 92–98.

[46] J. Zhu, Uncertainty of Kozeny–Carman permeability model for fractal heterogeneous porous media, Hydrology 10 (1) (2023) 21.

[47] B. Xiao, H. Zhu, F. Chen, G. Long, Y. Li, A fractal analytical model for Kozeny-Carman constant and permeability of roughened porous media composed of particles and converging-diverging capillaries, Powder Technol. 420 (2023) 118256.

[48] M.J. Yun, B.M. Yu, J.C. Cai, A fractal model for the starting pressure gradient for Bingham fluids in porous media, Int. J. Heat. Mass Transf. 51 (2008) 1402–1408.

[49] M.J. Yun, Seepage characteristics study on power-law fluid in fractal porous media, Math. Probl. Eng. 2014 (2014) 813561.

[50] P. Xu, A discussion on fractal models for transport physics of porous media, Fractals 23 (03) (2015) 1530001.

[51] S.S. Shapiro, M.B. Wilk, An analysis of variance test for normality (complete samples), Biometrika 52 (3/4) (1965) 591–611.

[52] D.W. Scott, On optimal and data-based histograms, Biometrika 66 (3) (1979) 605–610.

[53] H.A. Sturges, The choice of a class interval, J. Am. Stat. Assoc. 21 (1926) 65–66.

[54] ISO/IEC 17043:2023 - Conformity assessment. General requirements for the competence of proficiency testing providers (2023).

[55] W.L. Roque, K. Arcaro, A. Alberich-Bayarri, Tortuosity and elasticity study of distal radius trabecular bone, 7th Iberian Conference on Information Systems and Technologies- CISTI 2012, (2012), Madrid, Spain, pp. 1–4.

[56] W.L. Roque, K. Arcaro, A. Alberich-Bayarri, Mechanical competence of bone: a new parameter to grade trabecular bone fragility from tortuosity and elasticity, IEEE Trans. Biomed. Eng. 60 (2013) 1363–1370.

[57] C.L. Gaol, L. Ganzer, S. Mukherjee, et al., Investigation of clogging in porous media induced by microorganisms using a microfluidic application, Environ. Sci. Water Res. Technol. 7 (2021) 441–454.

[58] M. Lengyel, N. Kallai-Szab, V. Antal, et al., Microparticles, microspheres, and microcapsules for advanced drug delivery, Sci. Pharm. 87 (2019) 20.

[59] N. Waisbord, A. Dehkharghani, J.S. Guasto, Fluidic bacterial diodes rectify magnetotactic cell motility in porous environments, Nat. Commun. 12 (2021) 1–9.

[60] D. Brkić, P. Praks, Unified friction formulation from laminar to fully rough turbulent flow, Appl. Sci. 8 (2018) 2036.